

Chapter 11

The HD Block-Coil Dipole Program at LBNL



Gianluca Sabbi

Abstract This chapter reports on the HD program, a series of high field models exploring the block-coil layout for application to the arc dipoles for future high-energy colliders.

11.1 Introduction

The HD program is a series of block-coil model dipoles developed at the Lawrence Berkeley National Laboratory (LBNL) to explore Nb₃Sn technology at the highest possible field, for application in future energy frontier accelerators (Sabbi 2003). Table 11.1 shows a summary of the series. The first model (HD1) used a flat racetrack configuration to probe the fundamental characteristics of this approach. Two assemblies were tested in 2003–2004 using a shell-based support structure that, for the first time, included provisions for axial preload (Lietzke et al. 2004, 2005; Ferracin et al. 2005). The magnet achieved a coil peak field of 15.4 T, demonstrating that block-coils could effectively utilize the latest generation of Nb₃Sn wires to operate above 15 T, while coping with coil stresses approaching 200 MPa. The HD2 model (Fig. 11.1) focused on incorporating the main design features required for high-energy collider applications: a magnetically efficient layout; a clear aperture in the 40 mm range; a cost-effective fabrication process; and high field quality over the full operating range from injection to high energy (Sabbi et al. 2005; Ferracin et al. 2006, 2008). Five assemblies were tested in 2008–2009 (Ferracin et al. 2009, 2010). The HD2c test achieved 13.8 T in the bore, which, at the time of writing, is still the highest field recorded in a model dipole with accelerator-relevant bore size and field quality. Further progress was limited by repeated quenches at the boundary between the coil straight section and ends. The HD3 model attempted to address these issues through more accurate conductor positioning at the critical locations, but showed similar quench patterns, indicating the need for additional analysis and optimization (Cheng et al. 2013, Felice et al. 2013; Marchevsky et al. 2014).

G. Sabbi (✉)

Lawrence Berkeley National Laboratory (LBNL), Berkeley, CA, USA

e-mail: glsabbi@lbl.gov

© The Author(s) 2019

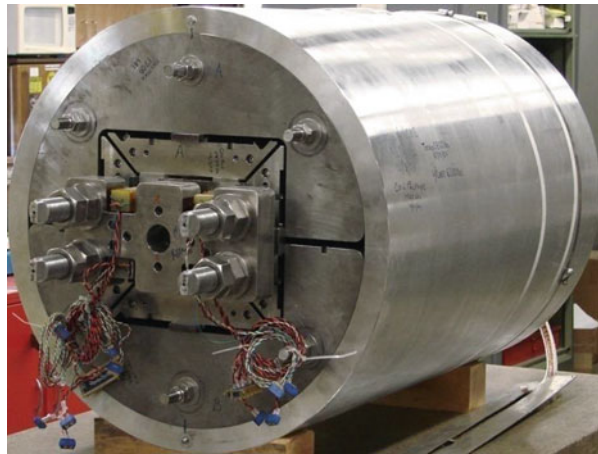
D. Schoerling, A. V. Zlobin (eds.), *Nb₃Sn Accelerator Magnets*, Particle Acceleration and Detection, https://doi.org/10.1007/978-3-030-16118-7_11

285

Table 11.1 HD model timeline, clear bore, and highest field at 4.5 K

Model	Year tested	Bore (mm)	B_{\max} coil (T)	B_{\max} bore (T)
HD1a	2003	8	15.3	16.0
HD1b	2004	8	15.3	16.0
HD2a	2008	36	14.0	13.3
HD2b	2008	36	14.0	13.3
HD2c	2008	36	14.5	13.8
HD2d/d2	2009	43	14.1	13.4
HD2e	2009	43	13.2	12.5
HD3a	2011	43	10.9	10.3
HD3b	2013	43	14.2	13.4

Fig. 11.1 HD2 magnet. This model (HD2c) achieved 13.8 T at 4.5 K, the highest value recorded to date in a dipole with accelerator-relevant bore and field quality

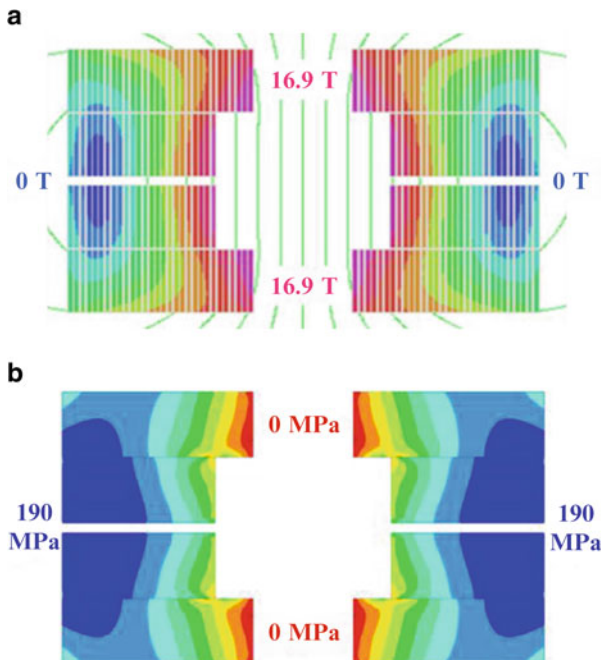


11.2 Block-Coil Dipole Design Features

The maximum field in superconducting accelerator dipoles depends primarily on the available current density and the coil width. When the coil width is relatively small compared to the required aperture, the traditional shell-type ($\cos\theta$) layout offers the most efficient solution (Mess et al. 1996). The arc dipoles of future colliders, however, enter a new regime of field, aperture, and forces that, coupled with the special properties of high-field superconductors, has prompted researchers at LBNL and elsewhere to explore alternative approaches (Sabbi 2002). Among these options is the block-coil layout, where a rectangular Rutherford cable is wound with its wide side parallel to the main dipole field.

A fundamental characteristic of the block configuration, compared to $\cos\theta$, is that the coil width is controlled by the number of turns rather than the number of layers. In the aperture range of interest for high-energy colliders, this feature can be exploited to access the highest field levels allowed by Nb_3Sn properties using only two layers, while meeting the most critical cable design, field quality, and coil fabrication requirements, and without introducing any internal spacers (Sabbi et al.

Fig. 11.2 HD2 coil cross-section showing the coil field map with: (a) flux lines; and (b) coil stress calculated assuming a 16 T target dipole field



2005). This solution, shown in Fig. 11.2, results in high efficiency and compactness, and minimizes the number of coil parts.

Another important feature of the block-coil winding orientation is the separation between the high field and high stress locations in the energized coil. The superposition of preload and Lorentz forces results in low stress in areas next to the bore, where the field is highest, while the highest stresses are located in the low field regions of the coil (Fig. 11.2). This characteristic can be exploited to minimize the impact of stress degradation on magnet performance.

Among the main technical challenges for the block layout is a reduction of the available aperture to provide structural support to the magnet bore. This is not the case in the cos-theta design, which exploits a self-supporting Roman arch layout using keystone Rutherford cables and wedges. In addition, a flared coil design needs to be developed to clear the beam path in the end regions while achieving high magnetic efficiency and field quality in the straight section.

11.3 HD1 Model

11.3.1 Magnet Design

HD1 was designed to explore the maximum dipole field that could be achieved using the best-performing Nb₃Sn wires available at the time. The magnet cross-section is

Fig. 11.3 HD1 magnet cross-section. The outer diameter of the shell is 74 cm

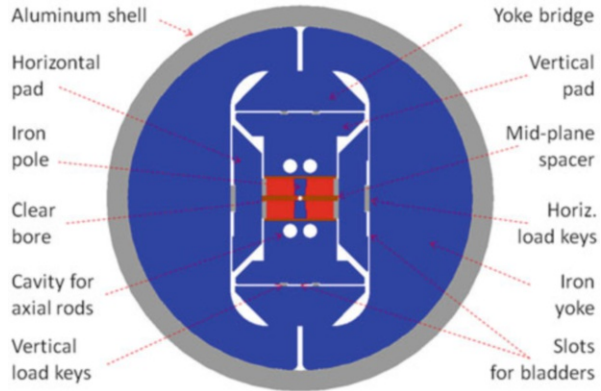


Table 11.2 HD1 design parameters

Parameter	Value
Strand diameter (mm)	0.8
Number of strands	36
Cable width (bare) (mm)	15.75
Cable thickness (bare) (mm)	1.40
Minimum bending radius (mm)	10
Cable insulation thickness (mm)	0.11
Number of turns (layer 1)	35
Number of turns (layer 2)	34
Mid-plane gap (total) (mm)	10
Clear bore diameter (mm)	8

shown in Fig. 11.3. Each pole is composed of a double-layer racetrack coil module wound from a continuous cable length around a 20 mm wide iron pole. A 10 mm thick G10 plate separates the coils and includes a small bore (8 mm in diameter) where the magnetic field can be measured using a Hall probe.

The conductor and coil parameters are listed in Table 11.2. The strand was produced by Oxford Superconducting Technology (OST) using the recently developed restacked rod process (RRP). The design was based on the 54/61 layout, with 54 hexagonal sub-elements composed of superconducting filaments embedded in a copper matrix, and seven sub-elements made of pure copper (Parrell et al. 2003). This conductor achieved a critical current density at the level of 3 kA/mm² at 12 T and 4.2 K, a significant improvement over previous generations. Cabling was performed at LBNL using a two-step process aimed at improving mechanical stability while minimizing damage to the sub-elements. The cable is initially fabricated with a thickness slightly larger than the final target. It is then annealed at 200 °C for 6 h and re-rolled to the final dimensions.

HD1 used a simplified coil design that severely limited the clear bore size and field quality, but retained the most fundamental technological challenges of high

field accelerator dipoles: high coil stresses, approaching 200 MPa; mechanical and magnetic forces acting primarily on the wide face of the cable and accumulating over many turns; and high axial forces in the end regions. In order to confront these challenges, a full 3D preload system was implemented. The support structure, shown in Fig. 11.3, is based on a thick aluminum shell surrounding the iron yoke, which is vertically split in two halves with an open gap. Inside the yoke, horizontal and vertical iron pads support the coils. The transverse preload is achieved using water-pressurized bladders inserted between pads and yoke to compress the coil pack and tension the shell. Interference keys are inserted to lock the pre-stress and allow for bladder deflation and removal. The thermal contraction differentials between yoke and shell are exploited to generate a large increase of the pre-stress during cool-down, preventing over-stress and possible conductor damage during the warm assembly step.

Axial preload is also provided to minimize longitudinal displacements under excitation. Aluminum rods connect stainless-steel plates pushing on the coil ends. The axial rods are pre-tensioned during assembly. Similar to the transverse preload system, thermal contraction differentials between the aluminum rods and the iron winding pole generate a substantial increase of the axial force during cool-down in order to reach the target preload.

11.3.2 Fabrication and Test Results

Lorentz force accumulation during magnet excitation is not a major concern in the block-coil geometry, since the highest stress occurs in a region where the field is low and a margin is available. A high coil preload is required, however, to prevent conductor motion under Lorentz forces. The mechanical stress associated with the preload can cause permanent degradation of the conductor properties, and limit the magnet performance. In addition, the stress variation during cool-down needs to be accurately predicted and monitored to avoid overshoot. For these reasons, a conservative preload target was selected in the first assembly of HD1 (HD1a). The shell azimuthal tension was 25 MPa at assembly and increased to 120 MPa after cool-down. The corresponding coil pre-stress was calculated to be 25 MPa at assembly and 155 MPa after cool-down (Ferracin et al. 2005). The HD1 shell and yoke were previously used for the RD series of common-coil dipoles, which generated a much higher horizontal Lorentz force. Therefore the shell thickness was larger than optimal, and resulted in most of the preload being generated by the cool-down differentials.

Based on the finite element analysis (FEA) results, the transverse preload of HD1a was expected to maintain contact at the coil–pole interface at up to 95% of the short sample limit. Magnet training (Fig. 11.4) started at a coil peak field of 12.8 T, and progressed to 15.2 T in 12 quenches (Lietzke et al. 2004). In this phase, most quenches were located in the return end, at the outer tip of a spacer introduced to reduce the peak field. Afterwards, training became more erratic and the quench

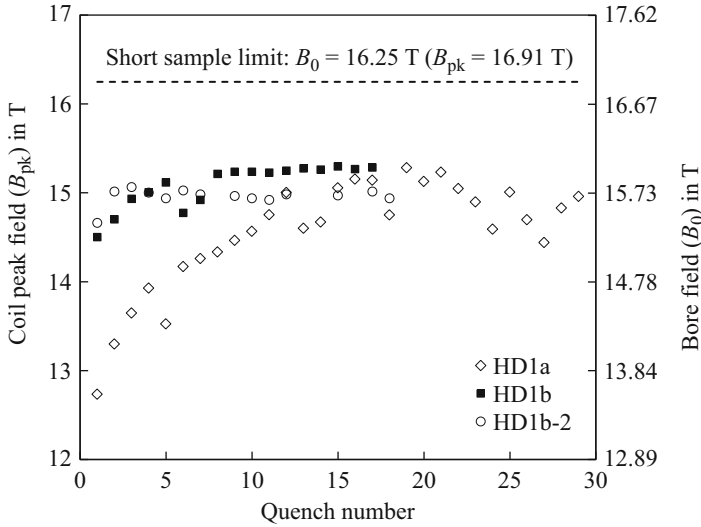


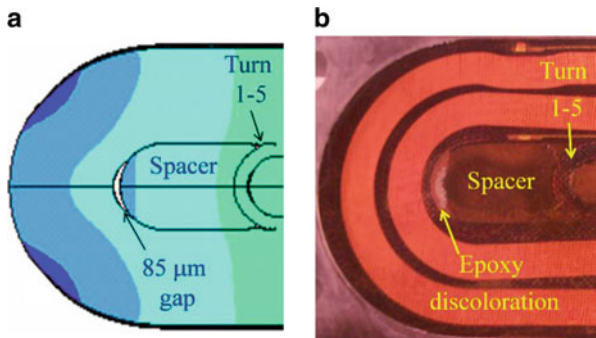
Fig. 11.4 HD1a, HD1b, and HD1b-2 training quenches at 4.5 K

locations shifted to the straight section at the high-field pole turn. The maximum coil field oscillated between 14.5 T and 15.3 T. The estimated short sample is 16.25 T, based on critical current measurements of extracted strands reacted with the coils.

A detailed analysis was performed following the HD1a test in order to understand and correct the observed limitations (Ferracin et al. 2005). The 3D FEA model showed a 15 μm gap developing during cool-down at the outer tip of the return end spacer, and increasing to 85 μm at the highest current achieved during the test. This behavior was attributed to a stainless-steel rail surrounding the coil and intercepting the axial preload. A similar but smaller gap (65 μm) appeared in the lead end, which featured an end shoe sliding between side rails. Increasing the axial force did not result in significant reduction of the computed gap. A reduction of the gap size by a factor of about 2 was obtained, however, by slightly reducing the rail thickness in a short segment at the end of the straight section. This relief allowed some bending in the side rail and facilitated the transfer of axial preload to the coil. A visual inspection of the coils performed after the HD1b test showed epoxy tearing at the coil-to-end-spacer interface, confirming the mechanical analysis results (Fig. 11.5).

The straight section quenches were attributed to non-uniformities in the coil transverse size, resulting in areas of low horizontal preload. In order to address this issue, shimming was introduced to improve the coil size uniformity. In addition, the coil preload was increased by 30 MPa, reaching a peak of 185 MPa. HD1b had faster training to a stable plateau with a field level close to the maximum reached in HD1a (Fig. 11.4). The initial quenches were again located in the end regions, while plateau quenches occurred in the highest field region and had the characteristics of a conductor-limited, rather than motion-triggered, origin. Following a thermal cycle, the magnet exhibited a stable plateau but at a 2% lower level than previously

Fig. 11.5 (a) HD1a coil displacements calculated for the actual preload conditions and maximum achieved current, showing a gap of $85\ \mu\text{m}$ between coil and spacer. (b) Picture of HD1 coil 1 showing epoxy discoloration and tearing at the coil-spacer interface. (Ferracin et al. 2005)



achieved. A temperature dependence study performed at the end of this test provided further confirmation of a conductor-limited plateau (Lietzke et al. 2005). These results indicate that the HD1b preload is at the limit for permanent critical current degradation. However, the HD1 demonstration of consistent performance at the 15 T level, achieved with fast training and no retraining, opened the way to the development of a new generation of high-field magnets enabling future colliders such as the High Luminosity Large Hadron Collider (Sabbi 2013) and the 100 TeV Future Circular Collider (Tommasini et al. 2017).

11.4 HD2 Models with 36 mm Bore

11.4.1 Magnet Design

The main goal of HD2 was further developing the block-coil approach for high-field dipoles by introducing a clear bore and field quality in the range required for high-energy physics colliders. The coil cross-section is shown in Fig. 11.6. Each pole is composed of a double-layer winding using a continuous cable length. In order to satisfy the design objectives with only two layers in each pole, a wide cable is required. In fact, the cable width should be comparable with the vertical aperture, so that the second layer can protrude toward the vertical axis to adjust the field quality, while the first layer can provide a high conductor packing factor in the region closer to the mid-plane. Due to the limited experience with the new RRP process, the strand diameter and layout was kept the same as in HD1, and the number of strands was increased up to the mechanical stability limit for coil winding. Following a series of cabling and winding tests, a 51-strand design was selected. The 22 mm cable width could support a coil aperture of about 45 mm on each side, and was compatible with a bending radius of 12.5 mm as required for layer 2. In recent years, the available diameter of high-performance RRP wires has increased to about 1.2 mm, with a corresponding expansion of the aperture range accessible with this coil layout (Sabbi et al. 2016).

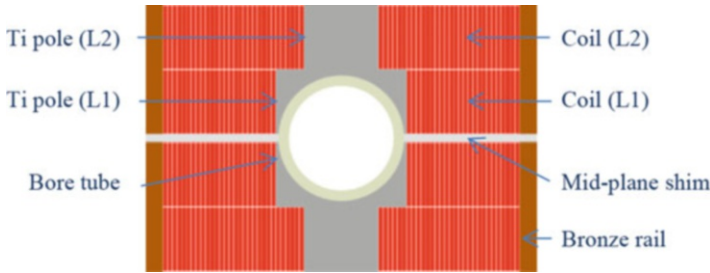
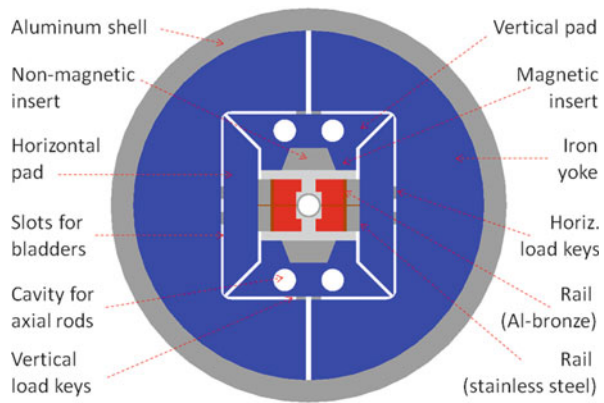


Fig. 11.6 HD2 coil module detail. The clear aperture is 36 mm in diameter

Fig. 11.7 HD2 cross-section showing the main coil and structural elements



The magnet cross-section is shown in Fig. 11.7. The iron yoke has an outer diameter of 623 mm. The coil field quality is optimized by adjusting the number of turns and positions of the two conductor blocks, without using internal spacers. This requires a mid-plane gap of 1.37 mm. In order to control the saturation harmonics, a spacer is introduced between the coil and horizontal pads, and inserts are placed between the coil and the vertical pads to create a trapezoidal iron profile.

A reference current of 16 kA, corresponding to a dipole field of 14.1 T, was chosen for optimizing the geometric field quality. The harmonic components, expressed in units of 10^{-4} relative to the dipole field at a reference radius of 13 mm, are: $b_3 = -0.13$, $b_5 = -0.20$, $b_7 = -0.09$, $b_9 = -0.89$. At a current of 2 kA, $b_3 = 4.06$, $b_5 = -1.15$. The harmonic variation due to the iron saturation effect from 2 kA to 16 kA is therefore $\Delta b_3 = -4.2$, $\Delta b_5 = +0.9$. This variation is monotonic and occurs in the first half of the current range, between 2 kA and 8 kA (Ferracin et al. 2008).

The coil peak field is located at the pole turn of layer 2, and the bore field to peak field ratio is 0.95. The main design and performance parameters are summarized in Tables 11.3 and 11.4. The coil field at short sample is about the same in HD2 as in HD1, while the bore field is lower by 1.4 T in HD2 due to its larger aperture and the use of a non-magnetic winding pole, as required to avoid a strong saturation effect

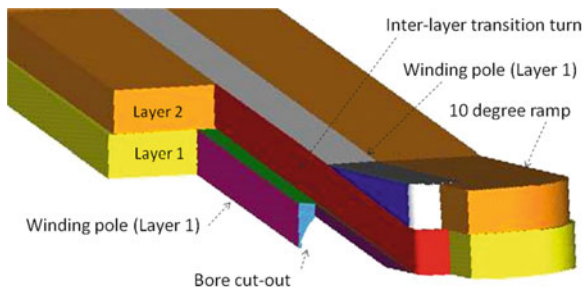
Table 11.3 HD2 design parameters

Parameter	Value
Strand diameter (mm)	0.8
No. strands	51
Cable width (bare) (mm)	22.000
Cable thickness (bare) (mm)	1.400
Insulation thickness (h/v) (mm)	0.110/0.110
No. turns/quadrant (layer 1)	24
No. turns/quadrant (layer 2)	30
Clear bore diameter (HD2a, b, c) (mm)	36.0
Clear bore diameter (HD2d, e) (mm)	43.3

Table 11.4 HD2 performance parameters

Parameter	HD2a, b	HD2c
Short sample current I_{ss} at 4.3/1.9 K (kA)	17.3/19.2	18.1/20.0
Bore field at I_{ss} (4.3/1.9 K) (T)	15.1/16.5	15.6/17.1
Coil peak field at I_{ss} (4.3/1.9 K) (T)	15.9/17.4	16.5/18.1
F_x/F_y layer 1 (quadrant) at 17.3 kA (MN/m)	+2.3/-0.4	
F_z layer 1 (quadrant) at 17.3 kA (kN)	90	
F_x/F_y layer 2 (quadrant) at 17.3 kA (MN/m)	+3.3/-2.2	
F_z layer 2 (quadrant) at 17.3 kA (kN)	126	
Stored energy at 17.3 kA (MJ/m)	0.84	
Inductance (mH/m)	5.6	

Fig. 11.8 HD2 end design concept. The pole turn of layer 2 proceeds parallel to the magnet axis and meets layer 1 at the end of the 10° ramp



during the ramp to high field. Further details on the cross-section design and performance parameters are provided by Sabbi et al. (2005) and Ferracin et al. (2006, 2008).

The main features of the coil ends are shown in Fig. 11.8. The design generally follows the D10 block-dipole (Fig. 11.9), which was the first Nb₃Sn magnet fabricated at LBNL and reached a bore field of 8 T (Taylor et al. 1985). A hard-way bend is introduced to ramp the conductor blocks away from the bore with a 10° angle. After the hard-way bend, a flat racetrack end configuration is recovered on the inclined plane. The transition from layer 1 to layer 2 is accomplished by continuing the pole turn of layer 2 parallel to the magnet axis. As the transition turn approaches



Fig. 11.9 Roy Hannaford winding the D10 coils (ca. 1983). The flared end and inter-layer transition of HD2 closely follows the concept developed for D10

the layer 1 elevation, a hard-way bend is included to match the angle of the ramp. The subsequent easy-way bend has two sections with different radii, the first using the layer 2 radius (12.5 mm), and the second using the layer 1 radius (22.6 mm). At the end of the easy-way bend, the transition turn has become the layer 1 pole turn and can follow the down-ramp into the straight section.

The peak field in the coil ends is easier to control in a flared configuration, due to the increased vertical separation between poles. Without optimization of the coil and iron design, however, the field at the tip of the layer 2 innermost turn would still be 1.5% higher than in the straight section. To lower the end field, the length of the ramp is adjusted to shift layer 2 by 20 mm relative to layer 1 (Fig. 11.10). In addition, the vertical pads transition from iron to stainless steel, and the iron insert above the coil is tapered following the end flare. As a result of these modifications, a 7% field margin is obtained in the end regions, without requiring internal coil spacers.

Figure 11.11 shows the dipole field profile on the magnet axis. The field is stable within 1 unit up to $z = 142$ mm, and is within 1% of the central field up to $z = 217$ mm. The coil geometric straight section ends at $z = 237.4$ mm.

A critical new element of HD2 is the bore structure required to react the preload applied to the coil. This component needs to be compatible with the coil fabrication process, maximize the aperture available to the beam, and minimize deflections and stress during assembly, cool-down, and excitation. After investigating alternative options (Sabbi et al. 2005) it was decided to rely on the combination of two main structural elements: winding poles, made of a titanium alloy, and a stainless-steel tube (Nitronic 40), inserted in a round cavity with 21.65 mm radius carved in the layer 1 winding pole. The winding poles are an integral part of each double-layer coil

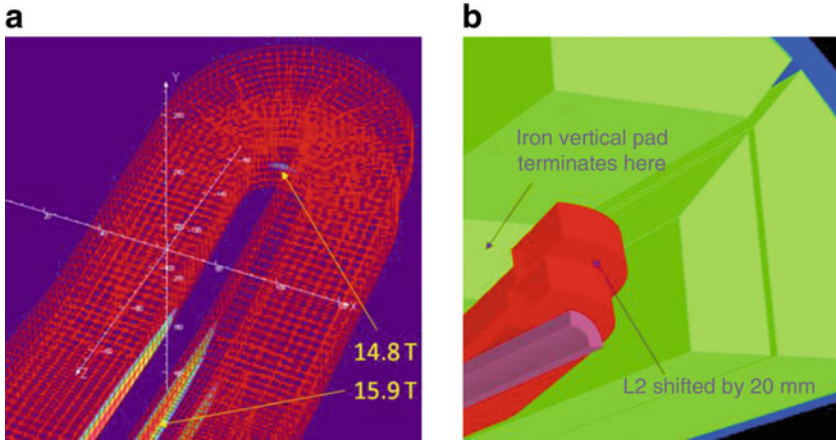


Fig. 11.10 Magnetic configuration of the end regions to reduce the peak field. (a) Peak field in the straight part and the end region; (b) iron configuration in the end region

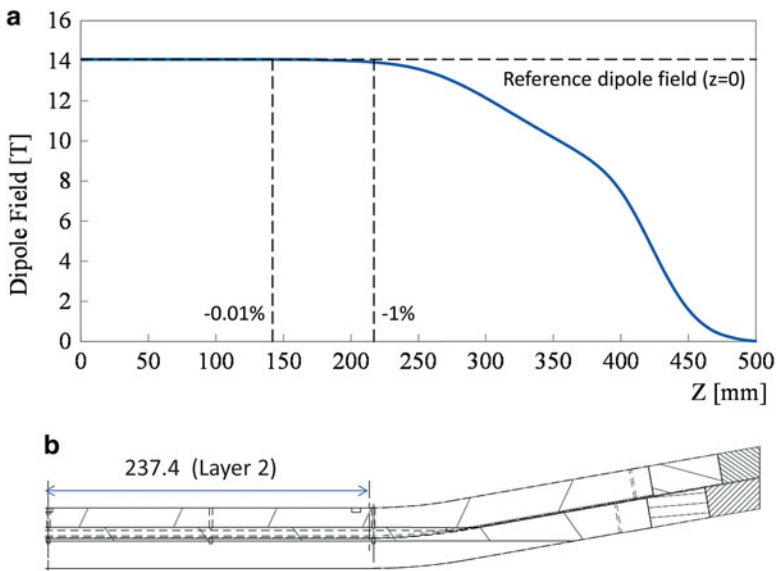


Fig. 11.11 (a) Longitudinal profile of the dipole field along the axis at 16 kA. The vertical lines indicate the longitudinal coordinates at which the dipole field decays by 0.01% (142 mm) and 1% (217 mm) relative to the central field; (b) a longitudinal section of the coil is also included for reference

and define its geometry. The central tube provides additional support in particular at the mid-plane, where the winding poles are thin and discontinuous. A conservative 3.65 mm wall thickness was selected for the first three assemblies of HD2, resulting in a clear aperture of 36 mm.

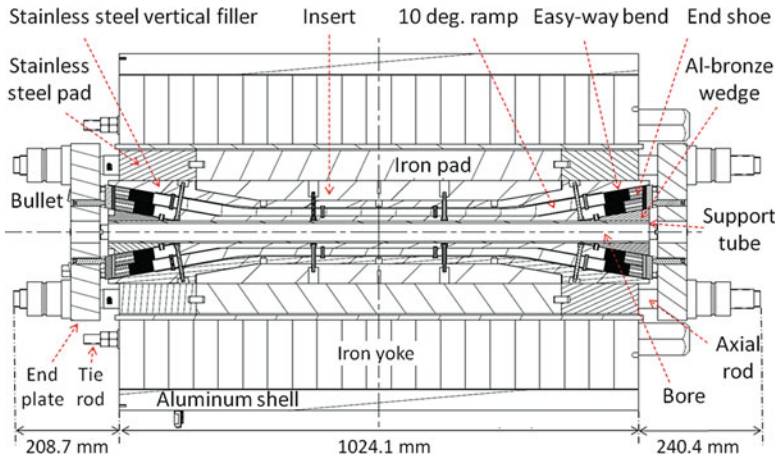


Fig. 11.12 HD2 longitudinal section showing the coil and structure elements

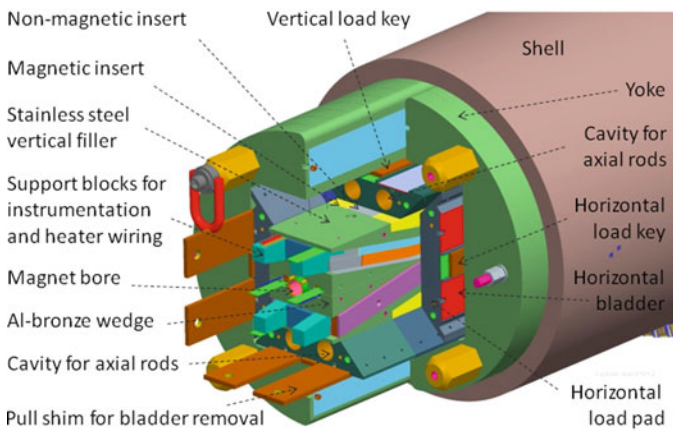


Fig. 11.13 HD2 CAD model with an exploded view of the main components

The external support structure is conceptually similar to HD1, but optimized for HD2 with all new components. The aluminum shell has an outer diameter of 705 mm and a thickness of 41 mm. Axial support and preload is provided by 50 mm thick stainless-steel endplates (Nitronic 40), connected by four 18.5 mm diameter aluminum rods. Details of the coil and structure design are shown in Figs. 11.12 and 11.13. Wedge-shaped elements surround the bore tube and support the flared ends on the bore side. The top surface of the coil is covered with a stainless-steel plate that also accommodates iron and stainless-steel inserts filling the cavity between end flares. These elements, labeled as “magnetic insert” and “non-magnetic insert” in Figs. 11.7 and 11.13, create a trapezoidal iron profile in the magnet cross-section, which is used to control the saturation harmonics.

Table 11.5 HD2 cable production data

Parameter	Coil 1	Coil 2	Coil 3
Cable ID	956R	966R	970R
Billet ID	7419, 7424	9770	9562, 9731
Strand diameter (μm)	802, 802	801	801, 804
Non-Cu fraction (%)	51.2	54.3	55
Reaction temperature (C)	668.9	679.5	678.4
Reaction time (h)	48	75	75
$J_c(15\text{ T}, 4.2\text{ K})$ (kA/mm ²)	1.72	1.90	1.88
Cabling degradation (%)	4.4	1.92	2.6
Production length (m)	130	135	115
Twist pitch (mm)	130	132.7	127
Thickness (first pass) (mm)	1.48	1.48	1.48
Thickness (final) (mm)	1.40	1.40	1.40

11.4.2 Magnet Fabrication

One practice coil and three production coils were fabricated for HD2. The first two assemblies (HD2a/b) used coils 1 and 2, while coils 2 and 3 were used in all subsequent assemblies.

Table 11.5 shows a summary of the cable production parameters, and Fig. 11.14 shows images of the fabricated cables. Coils 2 and 3 had significantly higher critical current density due to a change in the high-temperature stage of the heat treatment, from a nominal 665 C/48 h to 680 °C/75 h. The first two stages were the same for all coils: 210 C/72 h, 400 °C/48 h. The cabling degradation is about 4% in coil 1 and 2% in coils 2 and 3. These low values are consistent with scanning electron microscopy images showing minimal deformations of the sub-elements at the cable edges, a primary goal of the cable design and process optimization. Other parameters are similar for all cables. The finished cable lengths are in the 115–130 m range. The length of cable in one coil is 103.4 m.

The cable is insulated with a fiberglass sleeve of 0.11 mm thickness. Winding is performed starting from layer 2, using the stainless-steel filler as a base plate (Fig. 11.15). A 0.25 mm thick fiberglass sheet covers the base plate for electrical insulation. The winding spool is split in two portions, one for each layer. The winding pole is mounted on the base plate and the inter-layer transition is clamped in place. Layer 2 is wound, and the end shoes and side rails are installed. The same sequence is then repeated for layer 1, without an intermediate curing step. The coil pack is completed with end wedges and enclosed by reaction plates. End pushers are installed to maintain the end parts in position during reaction.

No axial pole gap is incorporated to release the winding tension and allow the coil to contract during the reaction process. With a flared end design, the tooling and parts should be designed to allow sliding in the straight section, while keeping the end components anchored to the coil. In order to simplify the design, it was decided

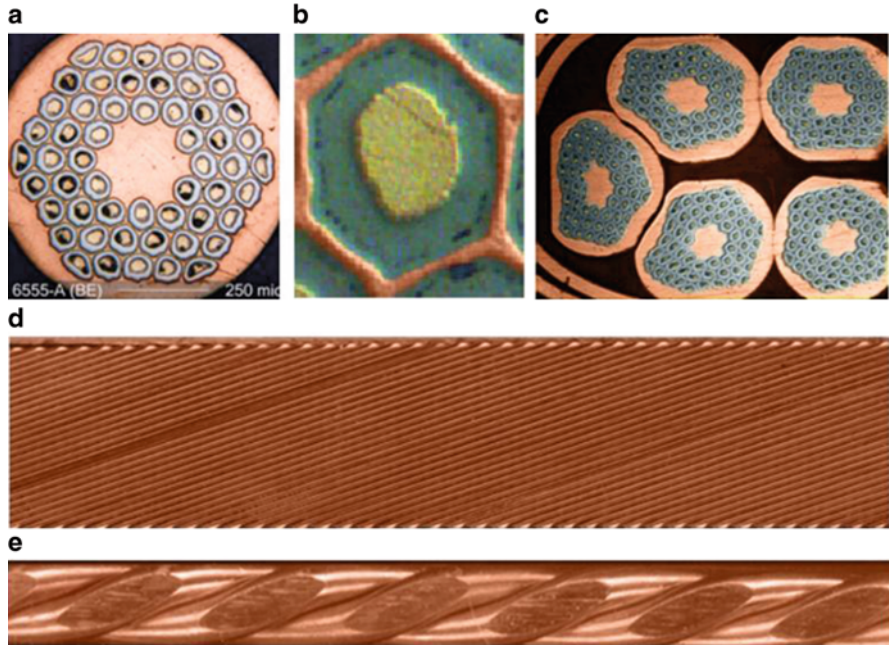


Fig. 11.14 HD conductor: (a) RRP54/61 strand used in HD1 and HD2; (b) sub-element detail; (c) cross-section of HD2 cable edge showing strand and sub-element deformations; (d) top view of HD2 cable; (e) side view of HD2 cable (not in scale with (d)) showing the flat surfaces (facets) at the layer transition

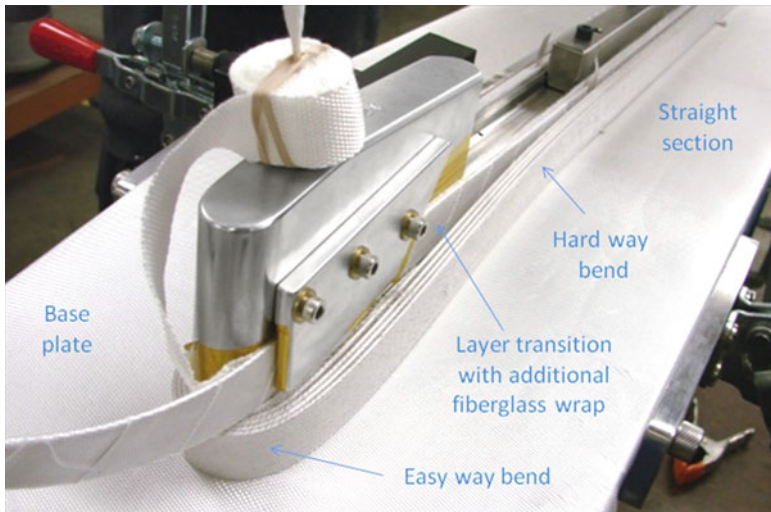


Fig. 11.15 Detail of HD2 coil winding, showing the base plate covered with a fiberglass sheet, the layer transition, and the first turns of layer 2



Fig. 11.16 HD2 coil: (a) top; and (b) bottom views. Two independent protection heaters are integrated in the instrumentation trace on each side of the coil

to delay implementing these features until a later phase in the program. Apart from this, the reaction process follows established procedures for Nb₃Sn magnets.

After reaction the instrumentation trace, integrating quench heaters with voltage tap and strain gauge wiring, are placed on the coil surface. The impregnation fixture is then assembled, sealed, and installed in a vertical position in a vacuum chamber. Epoxy filling takes place over a period of about 5 h, and is followed by a curing step. Figure 11.16 shows a picture of the completed coil.

In preparation for loading, the two coils are assembled around the supporting tube and mid-plane shim. The structure components up to the horizontal and vertical pads are added and bolted to form the coil pack. In a separate operation, the yokes halves are installed in the shell, pre-tensioned, and locked in place by temporary interference keys placed in the vertical gap. The coil pack is then inserted in the shell–yoke sub-assembly and bladders are installed in the horizontal and vertical gaps. An intermediate loading step is performed to compress the coil pack, tension the shell, and extract the yoke gap keys, replacing them with interference keys placed between pads and yokes. As a next step, the axial support system is installed, and the rods are tensioned using a hydraulic system. A final transverse loading step takes place to shim the interference keys and reach the design preload based on the strain gauge measurements.

11.4.3 Assembly and Test

The first HD2 assembly was initially cooled to liquid nitrogen to verify the FEA calculations. Tension increased from 49 MPa to 135 MPa in the shell, and from 34 MPa to 83 MPa in the rods. These results were consistent with the design targets, and no further modifications were required before the HD2a magnet cold test. At 4.5 K, the shell reached 144 MPa and the rods reached 90 MPa, corresponding to a

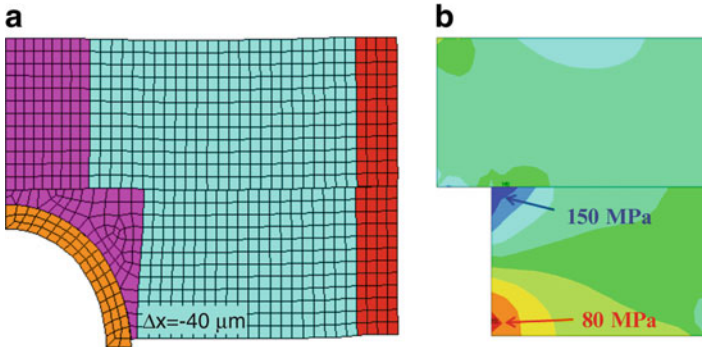


Fig. 11.17 (a) Coil deformation; and (b) stress at cool-down for a 14 T preload level

total force of 560 kN on the magnet ends. The calculated peak stress in the coil is about 150 MPa. Under these conditions, the coil–pole interface is expected to remain in contact up to a 14 T bore field. A minor adjustment of the coil end support was performed before the second test (HD2b) without unloading the shell. Details of the mechanical measurements and analysis are provided in Ferracin et al. (2009, 2010).

Figure 11.17 shows the calculated coil deformations and stress at cold. Due to the large thickness variation of the layer 1 winding pole, and the associated bending under the preload force, the peak coil stress is in the first turn of layer 1, at the corner away from the mid-plane where the winding pole deflections are at the minimum.

The training histories for HD2a and HD2b are shown in Fig. 11.18. HD2a had a first quench at 11.4 T (73% of I_{ss}). After 16 quenches it reached a maximum bore field of 13.3 T (87% of I_{ss}), with an estimated coil peak field of 14.0 T. In the second test (HD2b), the magnet did not exhibit memory of the previous training, and after a first quench at 11.0 T (71% of I_{ss}) it reached the same maximum field in 12 quenches.

Despite a significantly higher margin in coil 2, the HD2a quenches were evenly distributed between the coils. All quenches originated in the pole turn of layer 1, which has a 4% lower field with respect to the pole turn in layer 2, but significantly higher stress at cold (Fig. 11.17). The longitudinal locations, shown in Fig. 11.19, are concentrated at the end of the straight section, close to but before the start of the hard-way bend.

In the initial phase of the HD2b training, quench patterns were similar to HD2a (Lizarazo et al. 2009). In quench 12, however, a failure of the extraction system caused an increase of the quench integral released to coil 1 from 16 to 23 (kA)²s (million ampere squared seconds or MIITS). After this event, all quenches took place in coil 1, and three out of four were in the pole turn of layer 2 (peak field region). Higher ramp-rate sensitivity was also observed, and a reduction of the ramp rate from 20 A/s to 10 A/s was required to achieve the previous field level. These results indicate a degradation of the conductor properties of coil 1 due to the high temperature and stress experienced in quench 12.

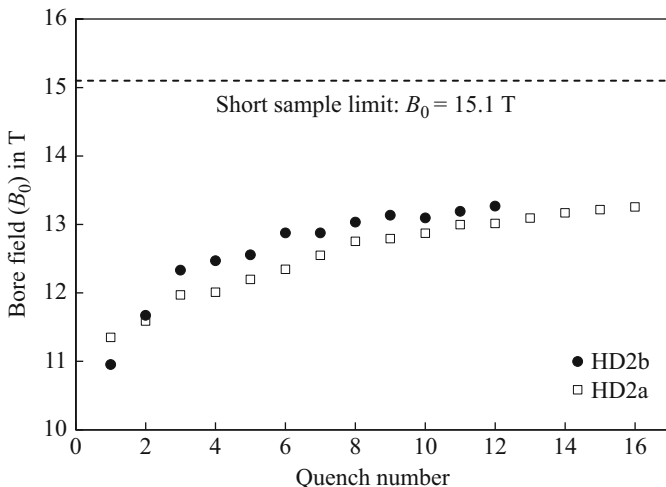


Fig. 11.18 Training quenches in HD2a and HD2b

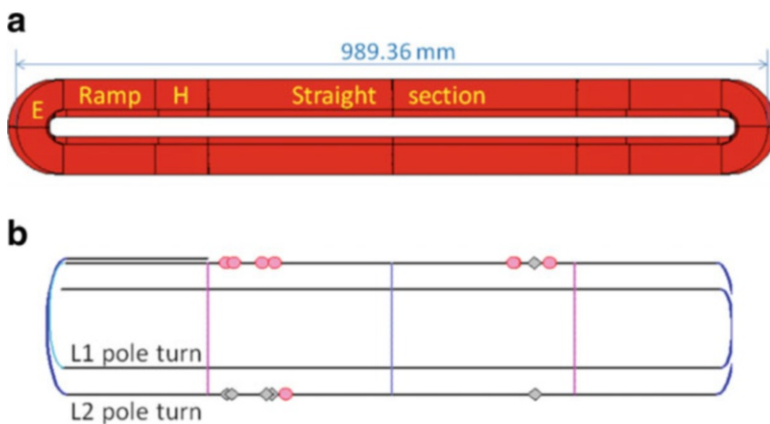


Fig. 11.19 HD2a longitudinal quench locations. (a) Schematic of coil: E: easy-way bend; H: hard-way bend; and (b) location of quenches. Coil 1 quenches are shown in grey; coil 2 quenches are in red

In HD2c, coil 1 was replaced by coil 3, matching the coil 2 performance and increasing the short sample field by 0.5 T. The shell tension was increased by about 13 MPa. A total of 28 training quenches were performed (Fig. 11.20). All 12 quenches in coil 2 started in the layer 1 pole turn, but were concentrated in a single straight section interval at the lead end transition side, within 100 mm from the start of the hard-way bend. In coil 3, two quenches started in the pole turn of layer 2, and 14 started in the layer 1 pole turn, at the lead end non-transition side, in a straight section interval of 50–100 mm from the hard-way bend. Quenches occurring in the layer 1 pole turn of one coil were often closely followed (within 1 ms) by an

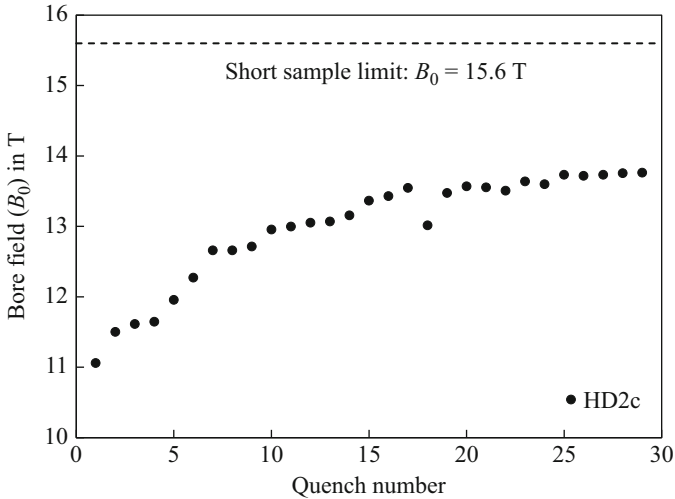


Fig. 11.20 HD2c training history and calculated short sample limit

adjacent quench in the layer 1 pole turn of the other coil, suggesting that the trigger event occurs in the vicinity of the mid-plane.

11.5 HD2 Models with 43.3 mm Bore

11.5.1 HD2d and HD2e Assembly and Test

After the HD2c test, the magnet was reassembled using the same coils, but without the bore tube. This configuration was not chosen to improve the performance, but rather to provide a benchmark for the mechanical analysis and characterization. In particular, it removed the uncertainty related to the contact between the tube outer diameter and the pole inner diameter, which is highly sensitive to fabrication tolerances, and made it possible to install strain gauges in the round cutout of the titanium pole.

Analysis showed that the layer 1 titanium pole could withstand the preload force, although deflections at the mid-plane increased by a factor of about 2, and the coil peak stress for a given shell tension also increased by about 15%. In order to maintain the peak stress at the level of previous tests, the shell tension was initially reduced to 130 MPa (HD2d) with a corresponding reduction of the field at which the coil would separate from the pole. In the next test (HD2e) a complementary case was studied by increasing the preload to the level required to maintain coil-to-pole contact up to 15 T, but at the risk of degrading the conductor under a calculated peak stress at cool-down of 185 MPa.

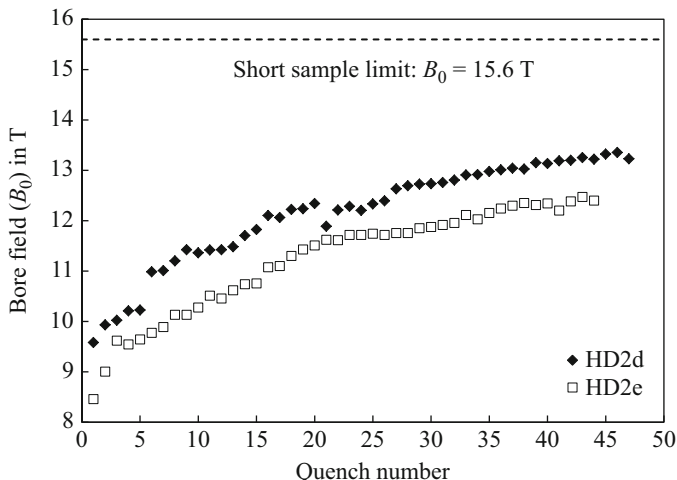


Fig. 11.21 Bore field (T) as a function of training quenches for HD2d and HD2e. The short sample bore field of 15.6 T corresponds to a coil peak field of 16.5 T

The quench histories are shown in Fig. 11.21. In the HD2d test, the magnet started training at a bore field of 9.6 T (59% of I_{ss}) and reached a maximum bore field of 13.4 T (84% of I_{ss}), corresponding to an estimated conductor peak field of 14.1 T, in 46 quenches. After increasing the coil preload in HD2e, the magnet trained from 8.5 T (52% of I_{ss}) to 12.5 T (74% of I_{ss}) in 43 quenches.

The locations identified in the HD2d and HD2e tests were at the pole turn of layer 1, in a segment of approximately 100 mm length at the end of the straight section, before the hard-way bend. While this is consistent with previous tests, training became significantly slower, and quenches were more widely distributed at the corresponding locations of both coils, both sides and both ends. In addition, the HD2e performance was about 1 T lower than HD2d, indicating further conductor performance degradation under the higher preload.

11.6 Analysis of HD2 Quench Performance

Most training quenches of the five HD2 assemblies originated in the layer 1 pole turn, within a short longitudinal interval at the end of the straight section, and at symmetric locations in both coils and both ends.

Quench evolution following the initial transition generally follows one of the following scenarios. In one case, a quench start is detected at an adjacent location in the layer 1 pole of the other coil. In the other case, a quench is detected in layer 2 of the same coil, at a location facing layer 1, without involving the highest field turns of layer 2 next to the pole (Ferracin et al. 2010).

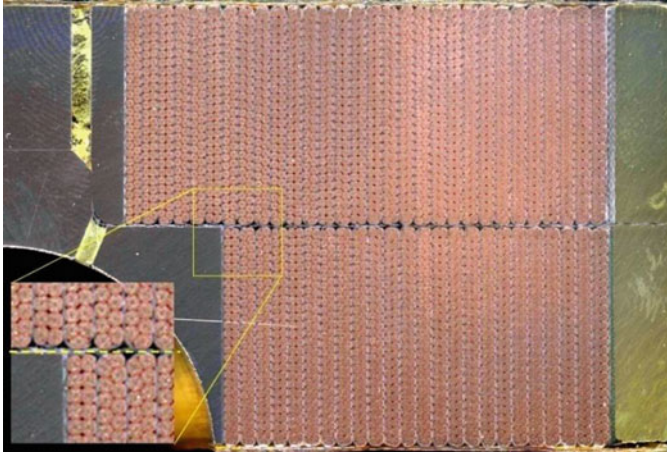


Fig. 11.22 Cross-section cuts of HD2 coil #1 in the center of straight section (Ferracin et al. 2010; Cheng et al. 2013). The two layers are close to the design positions

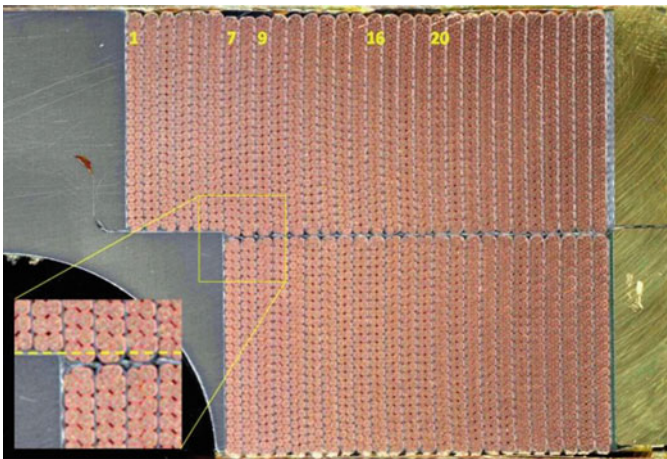


Fig. 11.23 Cross-section cuts of HD2 coil #1 at the end of the straight section, near the beginning of the end flare (Ferracin et al. 2010; Cheng et al. 2013)

Additional information is provided by images of coil 1 sections taken after it was replaced with coil 3. Figures 11.22 and 11.23 show a comparison of the cut at the magnet center, where no quenches were recorded, with the cut at the end of the straight section, where most of the quenches were located. In the latter, a shift toward the mid-plane can be noticed in the layer 2 turns after turn 6. The shift determines a compression of the layer 1 turns, and leaves a gap at the top of layer 2. The gap is filled with epoxy, indicating that the turn had already moved during the winding/ reaction stages, before impregnation. Turn 7 of layer 2 moves below the corner of the layer 2 island, creating the potential for stress concentration and insulation failure.

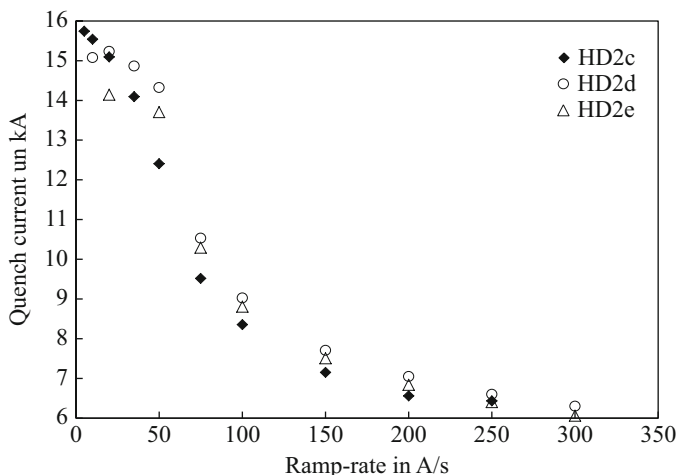


Fig. 11.24 Quench current as a function of ramp rate in HD2c, HD2d, and HD2e

Figure 11.24 shows the ramp rate dependence of HD2c, HD2d, and HD2e. In HD2c, the absence of a plateau at low ramp rate indicates that the highest quenches are conductor-limited. In HD2d, the maximum current is reduced from 16 kA to 15 kA, which may be attributed to the lower preload. Although fewer ramp rate measurements are available for HD2e, a comparison of the 20 A/s and 50 A/s points with the other two magnets appears to confirm the additional degradation of the conductor performance under the increased preload.

Summarizing the above findings, one can infer that two mechanisms are limiting HD2 performance: (a) stick-slip motions at the interface of the layer 1 first turn with the mid-plane spacer, where pole deflections and coil displacements are highest as the Lorentz forces acting on the turns balance the initial preload; (b) conductor degradation in the layer 1 first turn at the interface with layer 2, where the preload stress reaches its peak, and the conductor positions deviate from the design geometry. The lack of provisions to accommodate longitudinal coil expansion and contraction during reaction may be considered as an additional factor contributing to the HD2 stress degradation limit, which appears to be significantly lower than in HD1 (150 MPa vs. 185 MPa).

11.7 HD3 Models

11.7.1 Design and Fabrication

HD3 implemented several modifications aimed at better understanding and correcting the performance issues observed in HD2 (Cheng et al. 2013). The nominal coil envelope was unchanged, but the number of turns was reduced by one in each

Table 11.6 HD3 performance parameters

Parameter	Value
Short sample current I_{ss} at 4.4 K (kA)	18.67
Bore field at I_{ss} (T)	15.37
Peak field at I_{ss} (T)	16.26

layer. This change was implemented following the experience of the high-gradient quadrupole (HQ) models developed by the US LHC Accelerator Research Program, where it was found that previous criteria used to estimate the cable transverse expansion during reaction were not sufficient to prevent excessive strain and conductor degradation (Felice et al. 2012). Reducing the number of turns in the same coil envelope was the simplest and fastest route to provide additional transverse space, although the maximum field and field quality were negatively impacted (Table 11.6). The implementation of axial pole gaps to control the longitudinal strain during reaction was planned for the next set of coils, since it required more extensive modifications of coil parts and tooling.

In HD2, the hard-way bend connecting the straight section with the 10° end flare had a minimum bend radius of 349 mm (layer 2). Despite being more than 15 times larger than the cable width, this radius proved difficult to follow precisely during the winding process. As a consequence, the bend region extended into the adjacent straight section. The reaction and potting tooling and process helped to restore the desired geometry, but positioning errors were observed in the transition area after cutting HD2 coil 1 (Fig. 11.23). In order to avoid this effect, the hard-way bend radius of the HD3 coils was significantly increased to 873 mm. A curing step was also introduced after winding of each layer to help achieve and maintain the design geometry throughout the subsequent operations. The thickness of the fiberglass sheets used for inter-layer insulation and coil-pole insulation was increased for improved electrical robustness and to mitigate the effect of any residual positioning errors of the conductor. In order to ensure the correct axial positioning of the wedge-shaped spacers supporting the end flare, a mating surface was incorporated in the pole-island and the wedge.

Three coils were fabricated. One of them (coil 2) had to be discarded due to carbon contamination during reaction, leading to electrical shorts at several locations. Therefore, coils 1 and 3 were used in the assembly. The wire architecture was RRP 60/61 for coil 1 and RRP 54/61 for coil 3. The 60/61 wire had a copper fraction of 0.67, compared to 0.83 in the 54/61 wire. The critical current of the 54/61 wire was similar to previous HD2 coils. For the 60/61 wire, higher critical current density was found in virgin wires, but cabling degradation was also higher so that the critical current density of extracted strand measurements showed similar results as the 54/61. Nevertheless, the critical current (Fig. 11.25) was still considerably higher due to the larger area of superconductor relative to the stabilizer.

HD3 was assembled without a bore tube, similar to the last two tests of HD2. This approach facilitates the mechanical instrumentation of the pole, and the interpretation of the strain gauge data. It also provides a route towards larger clear apertures for given coil apertures, which is critical for collider applications. The inner radius of the

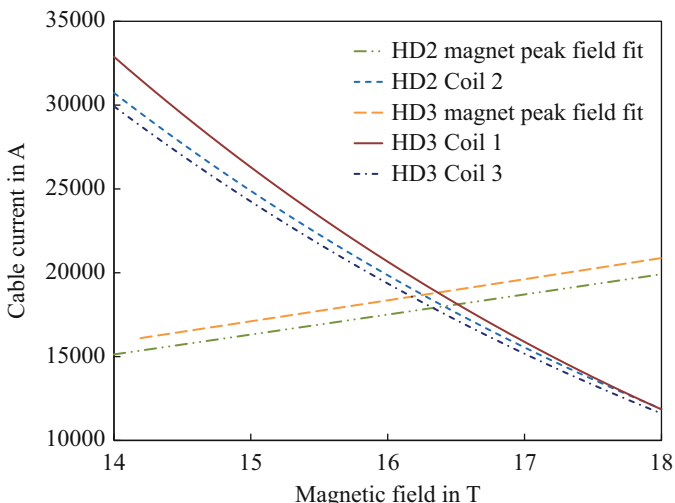


Fig. 11.25 Load line and critical current parametrizations of HD3 coils 1 and 3, and HD2 coil 2, at 4.5 K, based on measurements of extracted strands

round cutout for the pole-island of layer 1 was slightly reduced in HD3 from 22.3 mm to 21.5 mm, however, in order to reinforce the area close to the mid-plane. The main structure components were identical to HD2, and the preload targets were similar.

11.7.2 Test Results

The first test of HD3 (HD3a) had to be interrupted due to a short in the NbTi current leads. While the origin of this short was in the cryostat, the resulting arcing caused damage up to the NbTi–Nb₃Sn joints at the coil ends, requiring a complete magnet disassembly to perform a repair. In the second test (HD3b) two thermal cycles were performed. The training curves for the three tests are shown in Fig. 11.26. HD3a had a first quench at 6.5 T and progressed to 11.5 T in 14 quenches. HD3b started training just below 10 T and reached 13 T in about 45 quenches, after which progress became very slow. The maximum dipole field recorded was 13.4 T. After the thermal cycle, training started about 2 T higher and progressed to 13 T in five quenches. After that, progress became slower and seven additional quenches were required to reach 13.3 T. Therefore the magnet demonstrated some memory of the previous training, but the first quench was still substantially lower than the maximum level previously achieved, and recovering this level required significant retraining. Quenches were at the same locations as in the previous HD2 assemblies, indicating that improving the conductor positioning at the hard-way bend did not remove the HD2 performance limitations.

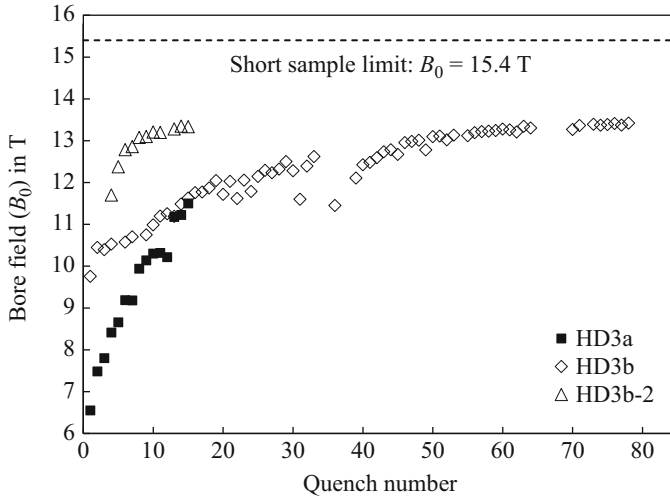


Fig. 11.26 Training histories of HD3a, HD3b, and HD3b-2 (second thermal cycle). (Marchevsky et al. 2014)

11.8 Summary and Outlook

The HD models represented an important step in the development of Nb₃Sn accelerator magnets for future high-energy colliders. Record fields were achieved in both technological (HD1a/HD1b) and accelerator (HD2c) configuration, coping with stress levels in the range 150–200 MPa. The coil design is magnetically efficient and requires only two layers per pole, with no spacers. Field quality features were implemented and a complete process for magnet fabrication was developed. Several critical questions, however, remain to be addressed.

First training was quite satisfactory for the first two assemblies of HD1 and HD2 using virgin coils. Both magnets achieved 80% of the short sample limit after two quenches, and progressed to 87% in 10–15 quenches.

After a preload increase, HD1b started training at 88% of the short sample limit and reached a stable plateau at the 95% level. Following a thermal cycle, the plateau level decreased by about 2%, but was achieved from the first quench.

Contrary to HD1, HD2 did not demonstrate a significant improvement of the first quench level in subsequent tests. The configurations including a bore tube had fast training to about 87% of the short sample limit, while those without a bore tube had significantly slower training. Based on these results, the bore tube or a thicker winding pole appears to be required, but the optimal configuration and thickness need to be further explored in order to effectively support the coil while preserving the largest possible aperture.

Analysis of the highest quenches in HD2 indicates that the magnet is ultimately limited by degradation of the conductor properties, rather than mechanical motion. The absence of a gap in the HD2 pole to control the axial strain during coil reaction, as typically implemented in Nb₃Sn magnets including HD1, is a possible factor

contributing to this degradation. A new set of tooling and coil parts was designed and procured to test this hypothesis (Cheng et al. 2013) but has not yet been used.

Achieving high dipole field in accelerator configuration was the main focus of the HD2 and HD3 models. Additional development will be required to fully satisfy the aperture and field quality requirements of future colliders. In particular, a 0.8 mm strand of the RRP 54/61 or 60/61 design was chosen for the HD models since it provided the best critical current performance. This layout, however, has a large effective filament diameter, which results in limited stability margins, and significant field distortions due to conductor magnetization (Wang et al. 2015). New wire architectures with a higher number of sub-elements should be implemented to increase the strand diameter and extend the design to a larger aperture while reducing the effective filament size (Sabbi et al. 2016). Compensation of the persistent current harmonics with thin magnetic inserts was also explored in the HD2 design (Ferracin et al. 2008). A detailed program of field quality characterization and correction was not carried out, however, and remains one of the main priorities for future development of the block-coil concept.

The extension of HD2 to a twin-aperture configuration, and the potential to reach higher field using grading, were explored by Sabbi et al. (2015). Detailed quench protection studies in accelerator conditions were also performed in recent years, with particular emphasis on the incorporation and optimization of the Coupling Loss Induced Quench (CLIQ) system to achieve a safe discharge in a broad range of design parameters and operating conditions (Ravaioli et al. 2016).

References

- Cheng DW, Caspi S, Dietderich DR et al (2013) Design and fabrication experience with Nb₃Sn block-type coils for high field accelerator dipoles. *IEEE Trans Appl Supercond* 23(3):4002504. <https://doi.org/10.1109/tasc.2013.2246811>
- Felice H, Ambrosio G, Anerella MD et al (2012) Impact of coil compaction on Nb₃Sn LARP HQ magnet. *IEEE Trans Appl Supercond* 22(3):4001904. <https://doi.org/10.1109/tasc.2012.2183843>
- Felice H, Borgnolutti F, Caspi S et al (2013) Challenges in the support structure design and assembly of HD3, a Nb₃Sn block-type dipole magnet. *IEEE Trans Appl Supercond* 23(3):4001705. <https://doi.org/10.1109/tasc.2013.2243794>
- Ferracin P, Bartlett SE, Caspi S et al (2005) Mechanical analysis of the Nb₃Sn dipole magnet HD1. *IEEE Trans Appl Supercond* 15(2):1119–1122. <https://doi.org/10.1109/tasc.2005.849508>
- Ferracin P, Bartlett SE, Caspi S et al (2006) Mechanical design of HD2, a 15 T Nb₃Sn dipole magnet with a 35 mm bore. *IEEE Trans Appl Supercond* 16(2):378–381. <https://doi.org/10.1109/tasc.2006.871323>
- Ferracin P, Caspi S, Cheng DW et al (2008) Development of the 15 T Nb₃Sn dipole HD2. *IEEE Trans Appl Supercond* 18(2):277–280. <https://doi.org/10.1109/tasc.2008.922303>
- Ferracin P, Bingham B, Caspi S et al (2009) Assembly and test of HD2, a 36 mm bore high field Nb₃Sn dipole magnet. *IEEE Trans Appl Supercond* 19(3):1240–1243. <https://doi.org/10.1109/tasc.2009.2019248>
- Ferracin P, Bingham B, Caspi S et al (2010) Recent test results of the high Nb₃Sn dipole magnet HD2. *IEEE Trans Appl Supercond* 20(3):292–295. <https://doi.org/10.1109/tasc.2010.2042046>
- Lietzke AF, Bartlett S, Bish P et al (2004) Test results of HD1, a 16 T Nb₃Sn dipole magnet. *IEEE Trans Appl Supercond* 14(2):345–348. <https://doi.org/10.1109/tasc.2004.829122>

- Lietzke AF, Bartlett SE, Bish P et al (2005) Test results of HD1b, an upgraded 16 Tesla Nb₃Sn dipole magnet. *IEEE Trans Appl Supercond* 15(2):1123–1127. <https://doi.org/10.1109/tasc.2005.849509>
- Lizarazo J, Doering D, Doolittle L et al (2009) Use of high resolution DAQ system to aid diagnosis of HD2b, a high performance Nb₃Sn dipole. *IEEE Trans Appl Supercond* 19(3):2345–2349. <https://doi.org/10.1109/tasc.2009.2019036>
- Marchevsky M, Caspi S, Cheng DW et al (2014) Test of the high-field Nb₃Sn dipole magnet HD3b. *IEEE Trans Appl Supercond* 24(3):1–6. <https://doi.org/10.1109/tasc.2013.2285881>
- Mess KH, Schmüser P, Wolff S (1996) *Superconducting accelerator magnets*. World Scientific, Singapore
- Parrell JA, Zhang Y, Field MB et al (2003) High field Nb₃Sn conductor development at Oxford Superconducting Technology. *IEEE Trans Appl Supercond* 13(2):3470–3473. <https://doi.org/10.1109/tasc.2003.812360>
- Ravaioli E, Ghini JB, Datskov VI et al (2016) Quench protection of a 16-T block-coil dipole magnet for a 100-TeV hadron collider using CLIQ. *IEEE Trans Appl Supercond* 26(4):1–7. <https://doi.org/10.1109/tasc.2016.2524527>
- Sabbi G (2002) Status of Nb₃Sn accelerator magnet R&D. *IEEE Trans Appl Supercond* 12(1):236–241. <https://doi.org/10.1109/tasc.2002.1018390>
- Sabbi G (2003) Nb₃Sn Magnet development at LBNL. In: *Advanced accelerator magnet workshop*, Archamps, 17–18 March 2003
- Sabbi G (2013) Nb₃Sn IR quadrupoles for the high luminosity LHC. *IEEE Trans Appl Supercond* 23(3):4000707. <https://doi.org/10.1109/tasc.2012.2233844>
- Sabbi G, Bartlett SE, Caspi S et al (2005) Design of HD2: a 15 Tesla Nb₃Sn dipole with a 35 mm bore. *IEEE Trans Appl Supercond* 15(2):1128–1131. <https://doi.org/10.1109/tasc.2005.849510>
- Sabbi G, Bottura L, Cheng DW et al (2015) Performance characteristics of Nb₃Sn block-coil dipoles for a 100 TeV hadron collider. *IEEE Trans Appl Supercond* 25(3):1–7. <https://doi.org/10.1109/tasc.2014.2365471>
- Sabbi G, Ghini JB, Gourlay SA et al (2016) Design study of a 16-T block dipole for FCC. *IEEE Trans Appl Supercond* 26(3):1–5. <https://doi.org/10.1109/tasc.2016.2537538>
- Taylor C, Scanlan R, Peters C et al (1985) A Nb₃Sn dipole magnet reacted after winding. *IEEE Trans Magn* 21(2):967–970. <https://doi.org/10.1109/tmag.1985.1063680>
- Tommasini D, Auchmann B, Bajas H et al (2017) The 16 T dipole development program for FCC. *IEEE Trans Appl Supercond* 27(4):1–5. <https://doi.org/10.1109/TASC.2016.2634600>
- Wang X, Ambrosio G, Chlachidze G et al (2015) Validation of finite-element models of persistent current effect in Nb₃Sn accelerator magnets. *IEEE Trans Appl Supercond* 25(3):1–6. <https://doi.org/10.1109/tasc.2014.2385932>

Open Access This chapter is licensed under the terms of the Creative Commons Attribution 4.0 International License (<http://creativecommons.org/licenses/by/4.0/>), which permits use, sharing, adaptation, distribution and reproduction in any medium or format, as long as you give appropriate credit to the original author(s) and the source, provide a link to the Creative Commons licence and indicate if changes were made.

The images or other third party material in this chapter are included in the chapter's Creative Commons licence, unless indicated otherwise in a credit line to the material. If material is not included in the chapter's Creative Commons licence and your intended use is not permitted by statutory regulation or exceeds the permitted use, you will need to obtain permission directly from the copyright holder.

